Graphite anodes for Li-ion batteries – an electron paramagnetic resonance investigation

Teresa Insinna,[1] Euan N. Bassey,[1,2] Katharina Märker,[1, 3] Alberto Collauto,[4] Anne-Laure Barra,[5,6] Clare P. Grey[1,*]

[1]Yusuf Hamied Department of Chemistry, University of Cambridge, Lensfield Road, Cambridge, CB2 1EW, United Kingdom

[2] Current address: Materials Research Laboratory, University of California, Santa Barbara, Santa Barbara, CA 93106-5121, United States

[3] Current address: Univ. Grenoble Alpes, CEA, IRIG, MEM, Grenoble 38000, France

[4]Pulsed EPR facility, Molecular Sciences Research Hub (Bldg C), 82 Wood Lane, Imperial College London, London, W12 0BZ, United Kingdom

[5]LNCMI-CNRS, EMFL, Univ. Grenoble-Alpes, 25 Rue des Martyrs, B.P. 166, 38042 Grenoble Cedex 9, France

[6]LNCMI-CNRS, EMFL, Univ. Toulouse 3, Insa Toulouse, 118 Route de Narbonne 31062 Toulouse Cedex 9, France

Abstract.

Graphite is the most commercially successful anode material for lithium (Li) ion batteries: its low cost, low toxicity and high abundance make it ideally suited for use in batteries for electronic devices, electrified transportation and grid-based storage. The physical and electrochemical properties of graphite anodes have been thoroughly characterised. However, questions remain regarding its electronic structure and whether the electrons occupy localised states on Li or delocalised states on C, or an admixture of both. In this regard, electron paramagnetic resonance (EPR) spectroscopy is an invaluable tool for characterising the electronic states generated during electrochemical cycling as it measures the properties of the unpaired electrons in lithiated graphite. In this work, *ex situ* variable-temperature (10-300 K), variable-frequency (9-441 GHz) EPR was carried out to extract the *g*-tensors and linewidths, and understand the effect of metallicity on the observed EPR spectra of charged graphite at four different states of lithiation. We show that the increased resolution offered by EPR at high frequencies (>300 GHz) enables up to three different electron environments of axial symmetry to be observed, revealing heterogeneity within the graphite particles and the presence of hyperfine coupling to ^{7}Li nuclei. Importantly, our work demonstrates the power of EPR spectroscopy to investigate the local electronic structure of graphite at different lithiation stages, paving the way for this technique as a tool for screening and investigating novel materials for use in Li-ion batteries.

Introduction.

Graphite is the most widely used anode material for Li-ion batteries, whose low electrochemical potential, low cost, low toxicity and high abundance make it ideally suited for a variety of applications, such as batteries for devices, transportation and grid-based storage.[1–4] It is associated with

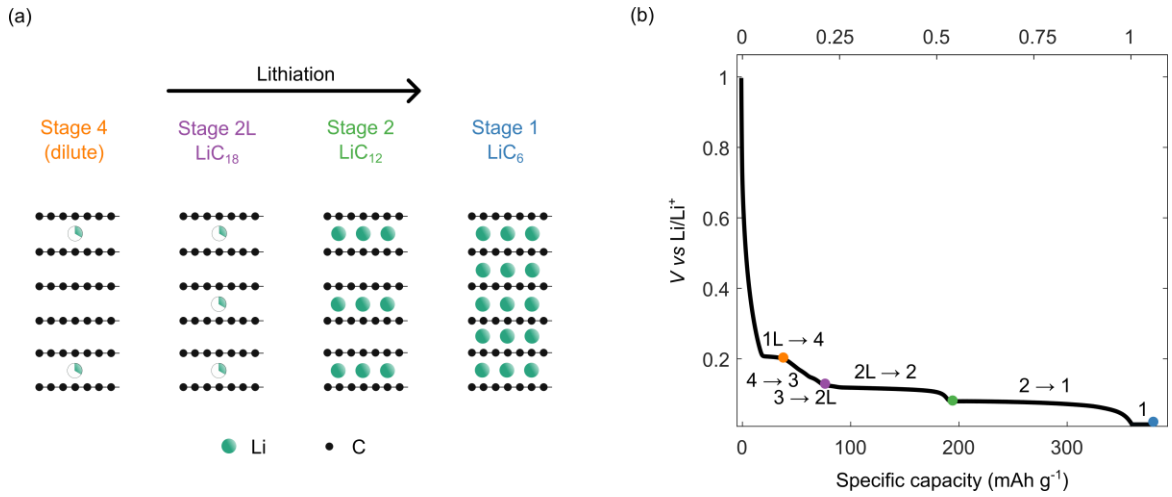

Figure 1 (a) Li intercalation stages as isolated in this work. The dilute stages are formed first (1L, followed by stages 4 and 3, the last two distinguished by the number of graphite sheets between the Li layers) up to 25% state of charge, after which the dilute stage 2 (2L) and the dense stages 2 and 1 form. In the figure above the interlayer spacing was kept constant for clarity, but as the concentration of Li^+ ions increases, the *c* lattice parameter increases by up to 10% (see main text). (b) Typical voltage profile for constant-current cycling of a Li:graphite half-cell. The transitions between intercalation compounds are indicated along the voltage profile and states of charge measured by EPR are indicated with colour-coded dots.

high capacities (372 mAh g^{-1}), which can be retained over many cycles, and is capable of hosting several different alkali metal cations in addition to Li.[5–9]

A range of mechanisms have been proposed in the literature that describe Li intercalation in graphite.[9–17] Among these, the Daumas-Hérold mechanism describes the lithiation of graphite as comprising at least four stages,[10] where the stage number indicates the number of graphite sheets between the Li layers;[9] for example stage 1 denotes LiC_6, comprising alternating layers of Li^+ ions and graphite sheets (Figure 1(a)). Stages formed above 0.076V *vs* Li/Li^+ are called "dilute" as only partial occupancy of Li sites between the graphite layers is found, while those formed below that potential are called "dense" (2 and 1, corresponding to LiC_{12} and LiC_6 respectively), the occupied Li layers being fully filled by Li.

This mechanism is now considered as simplified: subsequent work by Dahn[12] revealed the presence of additional dilute stages at low states of charge ($0.04< x< 0.3$ in Li_xC_6), and work by Ohzuku *et al.*[16] revealed the existence of a 'liquid' (or dilute) stage 1 (1L) prior to stage 4 and an additional stage 2L between stages 3 and 2 (Figure 1(b)). In these 'liquid-like' stages there is no visible Li ordering in the *a,b* planes.[15] These results were later confirmed using *in situ* ^{7}Li nuclear magnetic resonance (NMR).[13] More recently, *operando* neutron diffraction by Didier and co-workers[15] confirmed the presence of a hysteresis between lithiation and delithiation of graphite in the dilute stage region.

While the physical and electrochemical properties of graphite have been thoroughly characterised,[15–20] there are still open questions regarding the electronic structure of graphite: where are the electrons located in the different stages of lithiated graphite? Do they occupy localised states on Li, delocalised states on C, or an admixture thereof?

Perhaps the most convenient, non-invasive technique to study unpaired electrons is EPR spectroscopy, which probes unpaired electron spin microstates in an analogous fashion to nuclear spin microstates in NMR. The method has been applied to study, for example, Li metal dendrites and a number of cathode materials.[21–23] Here we use high and low field EPR to explore the electronic

properties of Li-intercalated graphite for battery applications. Our studies were performed on high performance, battery-grade graphite anodes, with the stages being isolated electrochemically to improve our understanding of graphite as an anode material. The graphite stages were isolated electrochemically by stopping the cells at the voltage cutoff of 0.20 V (nominally stage 4), 0.12 V (stage 2L), 0.076 V (dense stage 2) and 0.005 V (dense stage 1) *vs* Li/Li^+. Pulsed EPR (PEPR) was then used to measure electron relaxation times, while High Frequency (HF) EPR allowed to increase our signal resolution.

Unlike continuous wave (cw) EPR, where the electron spins microstates are excited under constant irradiation by microwaves, PEPR applies nanosecond-long microwave pulses to excite a region of the spectrum similar to conventional NMR spectroscopy, with the difference that the frequencies used here are of the order of GHz (not MHz) and that the pulse lengths are 3 orders of magnitude shorter (i.e., ns) than in NMR due to the faster relaxation times of electron spins and the need to excite a broader bandwidth. In contrast, HFEPR (performed in cw mode as it is more challenging experimentally to generate pulses at high frequencies are generally challenging) is a powerful technique to increase spectral resolution.

In the context of battery anode production, graphite is incorporated in electrodes together with other components—among them Super Porous (SuperP) carbon or carbon black. These components are typically added to increase the electrical conductivity within the electrode so that it can sustain faster cycling rates.[24,25] However, they are also EPR active and their signals overlap with those of the active material, altering the signal position, line-shape and linewidth. This work examines these components individually to separate their signals from those of graphite.

We show that combining cw and PEPR at variable temperatures (VT) and frequencies provides a more holistic picture of graphite's electronic properties. Lower frequencies (*ca.* 9 GHz, X-band) aid in the understanding of the bulk metallic structure of Li-intercalated graphite, while the higher frequencies provide a unique handle on the local electronic structure. We support our spectroscopic data with magnetometry to aid interpretation of the magnetic interactions present in these materials.

We begin this paper with a brief overview of EPR methodology as applied to metals, as EPR spectroscopy of metallic phases is less well described in recent literature; an understanding will be of particular importance for lithiated graphite.[26,27] We then provide a short overview of the EPR and electronic conductivity literature on pristine graphite and graphite intercalation compounds.

Background.

Electron Paramagnetic Resonance (EPR). In general, electron spin microstates are degenerate in the absence of a magnetic field but become non-degenerate under an applied magnetic field, $\boldsymbol{B}$, due to the electron Zeeman interaction:

$$h\nu = \mu_B \, \boldsymbol{g} \, \boldsymbol{B}, \qquad (1)$$

where h is Planck's constant, ν is the incident microwave frequency, μ_B the Bohr magneton and $\boldsymbol{g}$ the g-tensor, a second-rank tensor which is diagnostic of the local environment of unpaired electrons.

The principal components of the g-tensor reflect both the influence of spin-orbit coupling (SOC) on the energies of the electron spin microstates and nature of the orbitals that contain unpaired spin density:

$$g_{ij} = g_e \delta_{ij} - 2\lambda \Lambda_{ij}, \qquad (2)$$

where the first term describes the Zeeman splitting for a free electron (i.e., one which

does not interact with its surroundings), with g_e the free-electron *g*-factor (2.0023…) and δ_{ij} the Kronecker delta. The second term represents the SOC component of the *g*-factor, with λ the single-electron SOC constant and Λ_{ij} the integral representing overlap between ground and excited states which are coupled by the SOC interaction.[28,29] This second term is known as the *g*-shift and its value is inversely proportional to the energy difference between the ground and excited states being coupled *via* the SOC interaction. For strongly localised paramagnetic centres, a more than half-filled shell of electrons results in a negative SOC contribution, and therefore $g > g_e$, whilst a less than half-filled shell results in a positive contribution of the SOC and $g < g_e$.[30] In systems with delocalised orbitals, the *g*-factor depends on SOC, but also on band occupancy and the presence of defects and dopants.[31] It should be noted that a small change in *g* represents a very large difference in the resonance position: at X-band frequencies, a change in *g* of 0.01 corresponds to a difference in field position of 2 mT. Through the *g*-factor, EPR can thus provide useful information about the electronic structure (*via* the SOC component of the *g*-tensor) and the symmetry of the orbital containing the unpaired spin (isotropic, axial or rhombic).

The ability to excite conduction electrons in a metal is often reduced severely (Figure 2(a)): conduction electrons attenuate the microwaves, also causing phase shifts of the incident microwaves—a phenomenon known as the skin effect—with the distance into the bulk at which the amplitude of the microwave field is reduced by a factor of 1/*e* being termed the skin depth, δ:[26,32]

$$\delta = \left(\frac{c^2 \varepsilon_0}{\pi \nu \sigma}\right)^{1/2}. \qquad (3)$$

Here *c* is the speed of light, ε_0 is the vacuum permittivity, σ is the electrical conductivity of the metal and *v* is the applied microwave frequency. Only conduction electrons passing through the skin depth are irradiated; however, since they are mobile during the detection period the excited electrons can move out of this region, resulting in a decay of the signal. Hence, the spin concentration of a metallic sample cannot be simply determined from the double integral of the spectrum, unlike in systems with localised electrons.[33] For LiC_6, at X-band frequencies (*ca*. 9 GHz), δ ~1 μm (assuming an electrical conductivity of 2.4 ×10^5 S cm^{-1}, measured for transport in the *a*-*b* plane at room temperature)[6], while many graphitic particles are many microns in size (Hitachi MagE3 graphite has an average particle

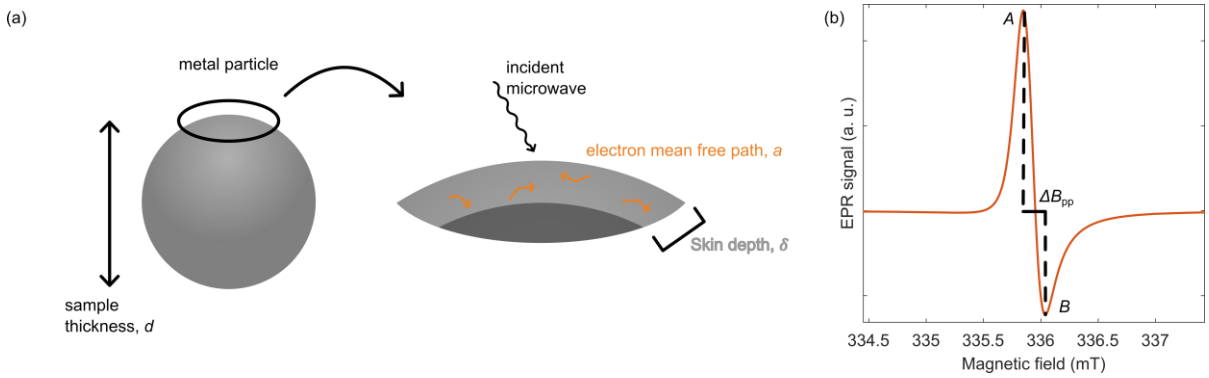

Figure 2. (a) Illustration of the skin depth of a generic metal particle with diameter, d upon incoming microwave radiation. (b)Typical EPR CW line-shape of conduction electrons in a metallic system. The intensity of the positive peak, *A,* is larger than the intensity of the negative peak, *B*, resulting in a Dysonian line-shape. The peak-to-peak linewidth, ΔB_{pp}, is also defined.

size of 13 μm, Figure S1). At the higher frequency of 331 GHz also used in this study, δ is even smaller, dropping to approximately 0.5 μm. The anisotropy in conduction and thus the skin depth is discussed in more detail later.

Skin effects can be classical or anomalous depending on the relative magnitudes of δ and the electron mean free path, *a,* i.e., the distance the electron travels before a collision with a defect in the lattice or with a lattice phonon occurs, the scattering process changing its velocity (and thus direction of travel). $\delta > a$ defines the classical scenario and $\delta < a$ the anomalous scenario, where electrons can travel in and out of the skin depth region multiple times before a scattering process occurs.[32] Anomalous skin effects are more likely as the temperature is decreased or the impurity concentrations are reduced, as *a* increases.

Metallic systems often exhibit asymmetric EPR resonances (Figure 2(a)), potentially providing further valuable information about the skin depth and thus the degree of metallicity. In the derivative spectrum, the asymmetry is quantified via an asymmetry parameter $A/B > 1$, *A* and *B* corresponding to the intensities of the positive and negative peaks, respectively, *B;* (in isotropic, non-metallic systems $A/B = 1$). This asymmetric line-shape is a consequence of both the fast movement of the electrons and the skin effect (Figure 2(b)), the electrons moving in and out of the skin depth region, during the CW irradiation, experiencing the CW irradiation at random intervals. The phase-shifted EPR line-shapes of metallic samples (Figure 2(a)) were modelled theoretically by Dyson[26] and then first observed experimentally by Feher and Kip.[27] Dyson considered a classical skin effect and modelled the lineshapes as a function of *skin* depth, δ, and sample thickness. The thickness to skin-depth ratio, d/δ, determines the A/B ratio and the contribution of absorptive and dispersive components to the observed EPR line-shape. The EPR line-shape of a very thin metallic film (i.e., $d << \delta$), has a dominant absorptive component (and is more symmetric), whereas that of a thick metallic film ($d >> \delta$) has a dominant dispersive component.[34]

A full analysis needs to consider multiple factors including the geometry of the metal particles and the *spin* depth, i.e., the distance an electron travels between spin flips; this distance is generally further than the average distance between collisions, *a*, (i.e., the mean free path of the electron) because not all collisions result in a change of spin. While a number of approaches have been taken to model these systems,[32] an important factor is the ratio T_D/T_{2e} (where T_{2e} is the transverse relaxation time of the electron or spin lifetime and T_D is the diffusion lifetime, defined as the average time taken for an electron to move in and out of the skin depth). T_D is a function of the skin depth, the velocity of the electron at the Fermi level, v_F, and the mean free path of the electron, *a*

$$T_D = \frac{3}{2}\frac{\delta^2}{v_F a} \quad (4)$$

T_D can be also expressed in terms of the skin depth (and thus the conductivity) and electron diffusivity, *D,* [32,35]

$$\delta = \sqrt{D\,T_D} \quad (5)$$

Of note, T_{2e} still sets the linewidth of the resonance, even if T_D is shorter than T_{2e}, the conduction electrons leaving and returning to the skin depth region multiple times during the time interval T_{2e}. As the skin depth decreases, the A/B ratio increases, reaching a maximum that depends on the T_D/T_{2e} ratio. For spherical particles and $T_{2e} >> T_D$ extremely large values of A/B can result when d/δ is large. For small values of d/δ, however, the A/B ratio is essentially independent of T_D/T_{2e} (see Figure 15 in ref[32]).

EPR and conductivity studies of graphite. EPR studies on pristine graphite were conducted in the 1950s and 1960s.[36–39] The first spectrum was collected by Castle[36] and contained a signal centred at g = 2.0083. A few years later, Wagoner carried out a more exhaustive EPR study on single crystals of graphite with Cu-covered edges to remove the signal from dangling bonds and isolate the signal coming from conduction electrons moving in the *ab*-plane.[37] The temperature dependence of the intensity was linked to Pauli paramagnetism, rather than Curie-Weiss paramagnetism, as the signal intensity increased linearly with temperature (analogously to polycrystalline graphite).[38] Additionally, the deviation of the *g*-factor from the free electron *g*-value (the *g*-shift) was temperature dependent, with smaller *g*-shifts at higher temperatures. This was explained by the increasing thermal population of states away from the band edge, which have a lower *g*-shift. This result agrees with theoretical work by McClure, which was based on band structure calculations and the position of the Fermi level.[39] Wagoner also showed that impurities result in the variations of the *g*-shift. For example, on adding boron atoms, the *g*-shift decreased with increasing B concentration.[37] This finding is counterintuitive based on simple molecular orbital theory arguments, as one would expect the *g*-shift to increase at higher B contents (due to the addition of holes into the bands). The *g*-shift can, however, be accounted for by considering that doping with boron lifts the degeneracy of the π bands in graphite, thereby increasing the energy gap between ground states and states that are coupled *via* the SOC interaction, thus decreasing the *g*-shift.[39] The temperature dependence of the linewidth revealed narrower line-shapes at higher temperature, which was attributed to motional averaging, typically caused by electrons moving across a large number of crystallites before losing coherence.[40]

The results obtained for single-crystal graphite were subsequently confirmed also in polycrystalline samples,[38] whose EPR signature revealed an noticeable *g*-anisotropy, linked with different electron mobility and conductivity in the *ab*-plane (within the layers) compared to the *c*-direction (perpendicular to the layers), which had not been probed in the single crystal studies. [37]

The electrical conductivity of graphite in the *a(b)*- and *c*-directions, σ_{ab} and σ_c, respectively, is substantially increased as Li ions are intercalated—electrochemically or chemically.[7] This is due to an increase in the number of charge carriers (introduced by reduction of graphite) and number of Li^+ between the layers.[8] While it is intuitive that these additional charge carriers improve the *ab*-conductivity upon lithiation, it is less obvious to understand how the overall conductivity anisotropy is affected. The latter is defined as σ_{ab}/σ_c, with values greater than 1 indicating preferential movement of electrons within the layers and values less than 1 between the layers. This ratio is considerably lower in Li-intercalated graphite than in other alkali-graphite intercalation compounds, a consequence of the small size of Li^+ ions: the interlayer spacing only expands by about 10% upon lithiation[4] and therefore the electrons introduced in the π^*-orbitals in the *ab*-planes are not fully decoupled from the adjacent layers.[6] Additionally, the intercalated Li^+ ions are thought to be partially involved in facilitating electrical conductivity in the *c*-direction *via* overlap of the C $2p_z$ orbitals with the Li 2*s* orbitals.[4,5,41]

If the particle size or sample thickness of graphite is larger than its skin depth (i.e., $d >> \delta$), the increase in the overall conductivity upon lithiation results in a decrease in the skin depth and consequently increased line-shape distortions in EPR spectra.[26,27,32] On a more practical note, the increasing electrical

conductivity upon charging is one of the reasons for the success of graphite in a lithium ion battery allowing moderately high charging rates.[24]

In the 1970s and 1980s, graphite intercalation compounds were of particular interest due to their potential as superconductors, resulting in a variety of studies assessing their physical properties and the tunability of the Fermi level *via* intercalating donors (such as Li, K, Rb, Cs) and acceptors (such as HNO_3, H_2SO_4, AsF_5).[6,7,42] Increasing donor size results in greater interlayer spacing as well as an increase in SOC and therefore electron relaxation rate (confirmed by broader EPR linewidths).[43,44] A major improvement to the understanding of the effect of donor species on the graphite density of states was achieved by Dresselhaus and co-workers, who concluded that the effect of increased SOC on the π band was to lift its degeneracy.[5,44] To the best of our knowledge, the only EPR study which covered at least three different lithiation stages of graphite was carried out by Lauginie and co-workers,[42] who compared the electronic properties of a range of HOPG donor and acceptor graphite intercalation compounds. This work builds on their study, extending to more disordered carbons and exploring the use high field and pulsed EPR spectroscopy.

Experimental.

Materials. Graphite electrodes were fabricated in the Argonne National Laboratory Cell Analysis, Modelling and Prototyping (CAMP) facility and are composed of 91.83 wt% graphite powder (Hitachi MagE3), 2 wt% carbon black (Timcal C45), 6 wt% PVDF binder (Kureha 9300) and 0.17 wt% oxalic acid; this mixture is coated on Cu foil. The areal loading of the graphite active material is 5.83 mg cm^{-2}. The graphite electrodes were punched out into discs (15 mm diameter), dried under vacuum at 120 °C for 12 h and then transferred to an Ar glovebox without exposure to air. The electrolyte used in this study was LP30 (1.0 M $LiPF_6$ in ethylene carbonate, EC:dimethyl carbonate, DMC, 1:1 v/v, battery grade, Sigma Aldrich). Li metal discs were purchased from LTS Research Laboratories, Inc. The separators used were glass microfiber (Whatman GF/B) cut into 16 mm disks. All procedures described below (coin cell assembly and disassembly, EPR capillary preparation) were performed in an Ar-filled glovebox with water and oxygen levels below 5 ppm.

Electrochemistry. All electrochemical tests were performed in graphite/Li half-cells in 2032 coin cells (Cambridge Energy Solutions). One graphite electrode disc, a glass fiber separator soaked with 100 µL LP30 electrolyte and one Li metal disc were stacked and assembled into the coin cell.

The cells were cycled galvanostatically (constant-current constant-voltage cycling, CCCV) at room temperature (20 ± 2 °C) on a VMP2 potentiostat (Biologic) at a rate of *C*/20 assuming a graphite capacity of 360 mAh g^{-1}. All potentials reported in this work are referenced against Li/Li^+.

The four different graphite stages were isolated after cycling the cells for 2 conditioning cycles at *C*/20 and then charging (lithiating) to a voltage cutoff of 0.20 V for stage 4, 0.12 V for stage 2L, 0.076 V for dense stage 2 and 0.005 V for dense stage 1. The cells were opened in a glovebox, the graphite electrodes extracted, rinsed with DMC and dried under dynamic vacuum for 15 min to remove excess solvent. The electrode materials were scraped off the Cu current collector, packed in quartz capillaries (1 mm diameter, Bruker) and sealed (two-component epoxy) for EPR characterization.

Solid-state NMR (ssNMR). Phase purity and the extent of lithiation were verified by ^7Li ss NMR. ssNMR spectra were acquired on a 11.74 T Bruker NMR spectrometer.

Samples were packed under Ar from cycled electrodes into 1.3 mm ZrO_2 outer diameter rotors. The MAS frequencies used were 30 kHz for the dense stages and 40 kHz for the dilute stages, and spinning was performed under N_2. Radiofrequency (rf) pulses used 125 kHz field strength for the dilute stages and 104 kHz strength for the dense stages, the pulse length being calibrated on sample due to metallicity. The chemical shift was referenced to solid LiF (−1.00 ppm). The spectra are shown in the SI (Figure S2).

X-band continuous-wave EPR spectroscopy. Ex situ cw EPR spectroscopy was carried out on an X-band benchtop EPR spectrometer (E5000, Magnettech) set at a microwave frequency of 9.477 GHz and equipped with a variable temperature (VT) unit connected to the cavity. The samples were loosely packed in to low-background 1 mm o.d. glass capillaries, although in one case (where noted, the sample packed in the NMR rotor was measured). A modulation field of 100 kHz was applied at 0.1 mT modulation amplitude. Except where otherwise stated, a microwave power of 5 mW was applied. VT experiments over the 300-100 K temperature range had a 10 K step between measurements and the temperature was allowed to equilibrate for 1 min before measurement.

Due to the Dysonian line-shape of the resonances, the *g*-factor cannot simply be read from the point at which the spectrum passes through zero intensity, but instead it was analytically extracted from the field corresponding to the centre of gravity of the spectrum;[32] we followed this procedure here.

High-frequency cw VT EPR spectroscopy. High-frequency (HF) cw EPR spectra were recorded on a double-pass transmission EPR spectrometer at the Laboratoire National des Champs Magnétiques Intenses (LNCMI, Grenoble, France).[45,46] The frequencies were varied from 331 to 441 GHz using two frequency sources (one operating at 127 GHz and the other at 110 GHz) and their multipliers, whilst detection was achieved using a bolometer. Temperatures were recorded using a variable-temperature insert (Cryogenic). The spectra were collected at 10 K, 25 K, 50 K, 140-170 K at the sweep rates reported in the SI (Table S1). The graphite powders were packed in 4 mm (outer diameter) Quartz tubes (Wilmad, Sigma Aldrich) and the powders were covered in nonane (99%, anhydrous, Sigma Aldrich) to prevent them from undergoing torquing effects (i.e., movement of the powders driven by the anisotropic susceptibility). The tubes were sealed using epoxy glue in an Ar-filled glovebox. Phase correction of the HFPER spectra was achieved through an in-house processing script using spherical harmonics. The EPR spectra were fitted to a powder pattern line-shape with anisotropic *g* using the EasySpin toolbox for MATLAB.[47] The fitted *g*-tensors were then corrected by using a field calibration factor obtained from a control sample (Mn^{2+} in MgO), as described further in the SI (Figure S3).[45] A phase fitting parameter in Easyspin was used to account for phasing caused by the skin depth.

Pulsed EPR spectroscopy. The Pulsed EPR (PEPR) measurements were performed at the Pulse EPR Facility based in Imperial College London using a Bruker Elexsys E580 X-band EPR spectrometer equipped with a 5-mm split-ring resonator (Bruker, model ER4118X-MS5-W) and a 1 kW TWT amplifier (Applied Systems Engineering Inc., model 117X). Temperature control was achieved using a closed-circuit cryostat (Cryogenic Ltd.).

FID-detected long-pulse saturation-recovery traces were recorded using the pulse sequence *sat–t–π*/2*–acq*, whereby the length of the *π*/2 pulse was set to 16 ns and the saturation (*sat*) pulse to 1 μs; all pulses had the same amplitude. A complete

16-steps phase cycle (cf. SI, Table S2) was used to suppress unwanted signals. The inter-pulse delay t was incremented in steps of 10 ns starting from a minimum value of 10 ns between the falling edge of the saturation pulse and the raising edge of the $\pi/2$ detection pulse. For each t value the whole FID transient was acquired with a 1.0 ns time resolution of the digitiser (Bruker, model SpecJet-III); the transients were integrated afterwards to yield the recovery traces; the extracted intensities were then fit to extract an apparent T_{1e}. The T_{1e}s were also measured using an inversion recovery (π –t–$\pi/2$–acq) sequence and similar values were obtained.

All pulse experiments were performed at the maximum of the EPR line. The repetition time was set to 100 µs (FID) or 200 µs (saturation recovery). The microwave pulses were generated using the SpinJet AWG unit (Bruker); the individual pulse phases (+x, +y, −x, −y) were calibrated at each temperature (Table S2).

Results

Pristine Graphite and Battery-Grade Carbons

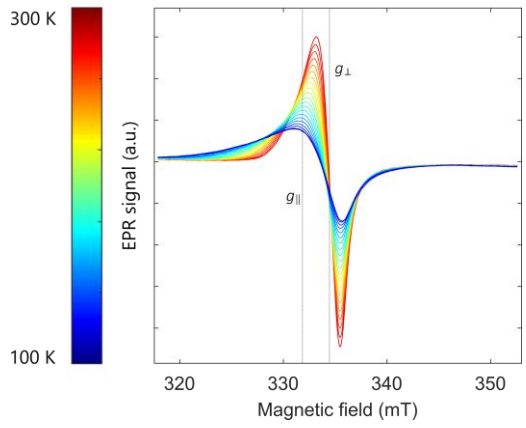

Figure 3. Variable temperature X-band EPR spectra of pristine Hitachi MagE3 graphite taken from 100 K (blue) to 300 K (red) in temperature steps of 10 K at 1 mW microwave power. The linewidth increases as the temperature decreases and the $g_\parallel$ component moves to higher g values/ lower magnetic field. The g values measured at 300K are marked.

Cw X-band VT EPR spectroscopy. We begin with a brief examination of the pristine graphite material. The room temperature X-band EPR spectrum of pristine graphite (Hitachi MagE3) contains a single line at g = 2.0319 (Figure 3, red trace). The signal is attributed to thermally excited electrons in the conduction band and/or defect spins from surface dangling bonds.[31,37] Owing to the axially symmetric crystal structure (a = b = 2.462 Å, c = 6.720 Å),[48] it is anticipated that unpaired electrons in graphite would give rise to an axial signal. The reason why no discontinuities are clearly resolved (i.e., why separate xy and z components are not seen) likely stems from the low frequencies used at X-band, resulting in significant overlap of the components of the g-tensor, $g_\parallel$ and $g_\perp$ corresponding to components in- and out of the plane of the graphite layers.[31] On cooling from 300 K down to 100 K, the signal broadens (from a peak-to-peak linewidth of 0.8 mT at 300 K to 2.4 mT at 100 K), which is at least in part ascribed to the reduction in motional averaging of signals from the different environments at low temperatures.[40] The spectra were fitted by including both $g_\parallel$ and $g_\perp$ (Figure S4), the $g_\parallel$ component shifting to higher g, from 2.04±0.02 at 300 K to 2.07±0.05 at 100 K (the error is obtained from the g strain used to fit the resonances) as observed by others[37,38,49]; $g_\perp$ remains around 2.02 (2.023±0.006 at 300 K to 2.025±0.005 at 100 K).

The EPR profiles of the conductive carbon species used in electrode fabrication are given in the SI (Figure S5). Briefly, carbon black has an axial signal ($g_\parallel$ = 2.04±0.02 and $g_\perp$ = 2.0182±0.0001) whilst SuperP carbon is isotropic (g_{iso} = 2.0154), the signal likely containing a significant contribution from defect spins within the carbon framework. The signals of these carbon additives are also shifted to higher field compared to graphite, consistent with the observation that more electronically conductive compounds with partially filled conduction bands result in a higher g-

factor.[31] In the electrodes used in this work, conductive carbon is present as 2 wt% (cf. Experimental section). Given the very low EPR signal intensity per mass and that we are not aiming to extract quantitative information concerning the number of electron spins from our samples, the contribution of these electrode components to the battery anodes was not considered further in this work.

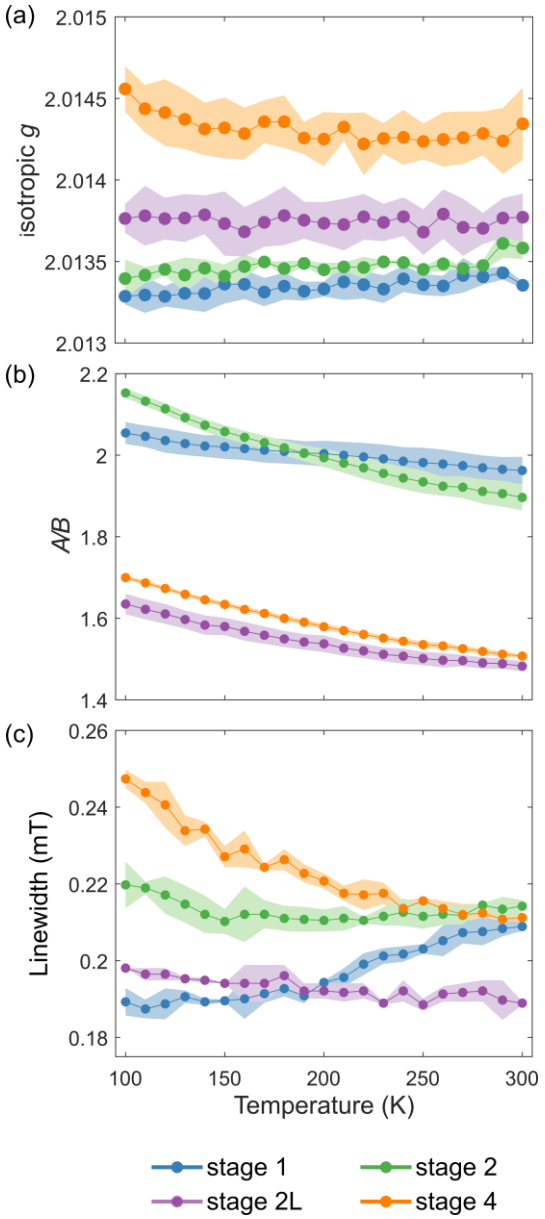

Figure 4. Temperature dependence of the isotropic *g*-factor (a), *A/B* ratios (b) and peak-to-peak linewidth (c) for the four lithiation stages of graphite. These parameters were extracted from resonances obtained at X-band in the temperature range 100-300 K with a temperature increment of 10 K. The shaded area represents errors derived by taking the range across 4 separate samples per lithiation stage.

Variable temperature *X-band* EPR of the four graphite stages was performed and an example of a variable temperature series is shown in Figure S6 (for stage 2), and the X-band spectra at 100 K of the four stages are shown in Figure S7. On lithiation of graphite (i.e., intercalation of Li^+ ions and adding electrons to the conduction band of graphite), the *g*-factor shifts towards g_e, from 2.0319±0.0005 (graphite) to 2.0144±0.0003 for stage 4 to 2.0133±0.0001 for stage 1 (Figure 4(a), Figure S5) at 300 K a consequence of the greater contribution of the Li 2*s* band to the Fermi level, and therefore a decrease of the SOC component. The *g*-factor remains approximately constant across the temperature range 100 K to 300 K for all states of charge (Figure 4(a)), consistent with the population of ground and excited states being temperature-independent around the Fermi level in metals.[32] Only isotropic *g*-factors were extracted for these resonances due to anisotropy not being resolved at these lower frequencies.

For all states of charge, the asymmetry parameter *A/B* was higher at lower temperature (Figure 4(b)), consistent with metallic systems where the electrical conductivity increases with decreasing temperature, leading to a decreased skin depth (Equation (3)). For the same sample temperature, the values of *A/B* indicate that stages 1 and 2 are the most metallic, whilst stages 2L and 4 are less metallic. We note that stage 2 has a higher *A/B* ratio (i.e., is more metallic) than stage 1 below 180 K. We ascribe this to the decrease in interlayer spacing (as temperature is decreased, as seen for pristine graphite)[50]—the degree of layer collapse being greater in stage 2 due to the presence of alternating Li-deficient layers. We note that care should be taken in comparing *A/B* ratios between samples as these values are also dependent on how

densely packed the samples are. For example, a sample of LiC_6 tightly packed in an NMR rotor gave rise to a signal with an *A/B* ratio of 3.80 (vs. 1.96, as measured in the more loosely packed capillary; see Figure S8), at room temperature. Thus, the skin depth and thus ability to excite the bulk sample is not only a function of the individual particle size but also of the extent of agglomeration of particles.

The linewidths of EPR signals can provide insight into a series of effects—principally the T_{2e} relaxation, the distribution of environments in the sample and electron mobility.[30] For stage 4, the linewidth obeys a similar temperature dependence as pristine graphite, where the linewidth becomes sharper as the temperature increases (Figure 4(c)). A similar trend is seen for stage 2L, but trend is noticeably less pronounced and the linewidths are considerably smaller (at 100 K, *ca.* 0.2 mT in stage 2L compared to 0.25 mT in stage 4; Figure 4(c)). ^{7}Li NMR measurements indicate higher Li^+ mobility in stage 2L than dense stages,[51] the EPR results similarly suggesting motional averaging of the electronic environments as the temperature is increased. The trend is opposite for stage 1, the linewidth, somewhat surprisingly, decreasing with temperature and plateauing at around 150 K. Stage 2 shows a more complex trend in which the linewidth initially decreases very slightly on cooling, but then increases more noticeably, the turnover occurring at 150 K. The increase in linewidth at low temperatures is tentatively assigned to the onset of magnetic exchange interactions (that become more important at low temperatures) as discussed below.

Pulsed EPR. Overall, determining the relative contributions of T_{2e} relaxation, distribution of environments and electronic mobility to the linewidth is challenging, but can be helped by using pulsed EPR measurements. Unfortunately, only the measurements of the longitudinal relaxation times, T_{1e}, were successful in these systems: measuring the transverse relaxation times, T_{2e}, requires a spin-echo sequence, where a delay is applied between the 90° and 180° pulses and prior to acquisition. If the T_{2e}s are very short, as observed here, all signal is lost before acquisition starts.[52]

The T_{1e}s for the four different stages were measured in the temperature range 10-300 K (Figure 5(a)) at X-band. For all stages, T_{1e} increases as temperature

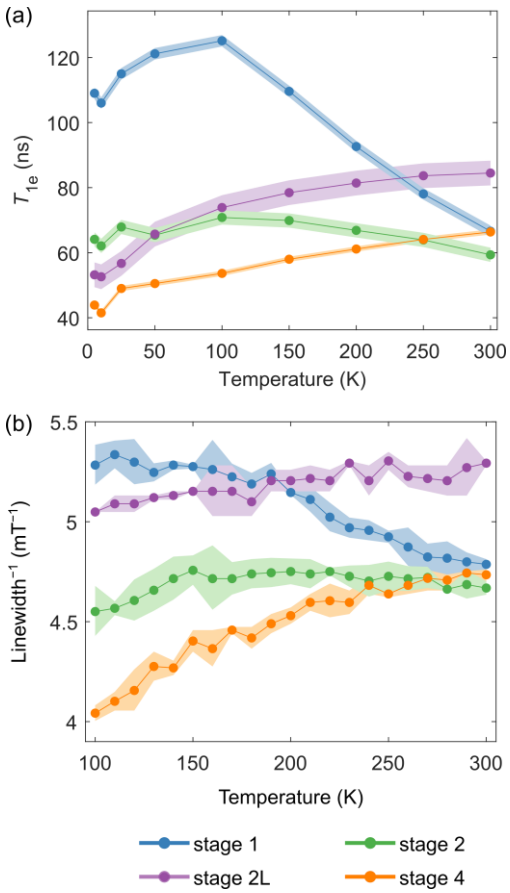

Figure 5. (a) The temperature dependence of the electron longitudinal relaxation times (T_{1e}) as measured by PEPR for the four lithiation stages of graphite between 10-300K. Two different trends for the dilute and the dense stages are seen, with the former increasing with temperature and the latter peaking at approximately 100 K to then decrease as the temperature increases. (b) Inverse of the linewidth (reported in Figure 4(c)) for the 4 lithiation stages of graphite as measured by cw EPR in the 100-300 K range. The linewidths are strongly affected by the T_{1e}.

increases in the region 10-100 K (Figure 5(b)). At temperatures above 100 K, this trend continues for the dilute stages but not for the dense stages, where instead a noticeable decrease in T_{1e} with increasing temperature was observed (particularly for stage 1). The inverse linewidths are plotted in Figure 5(b) and they mirror the trends in the T_{1e}s with temperature, and again different trends are seen for dilute and dense stages.

What is surprising is that the linewidths measured by CW EPR are sharper than those predicted based on the measured T_{1e}s. For example, a T_{1e} of 66 ns (the value for stage 1 at room temperature) leads to an estimate for the linewidth of 1.07 mT, assuming that the T_{2e} is determined by the T_{1e}. At 100 K a T_{1e} of 125 ns corresponds to a calculated linewidth of 0.57 mT. The origin of these differences is discussed below.

Magnetic susceptibilities. The bulk magnetic susceptibilities for each stage were measured in order to help separate contributions to the EPR signals from metallic (Pauli)-like vs. localised spins and to explore whether magnetic exchange interactions are responsible for some of the observed behaviour. Stage 4 shows a diamagnetic response, while the other three are weak paramagnets. A turnover in the zero-field cooled (ZFC) susceptibility at 15 K and 25 K is seen for stages 1 and 2, respectively (see Figure S9). A Curie-Weiss fit of the χ vs T plot for stage 1 (above 150 K, i.e., in the Curie-Weiss region) results in a Weiss constant θ = −88 K, suggesting spin alignment starts around the turnover temperature seen in the T_{1e} data. Temperature-dependent (or Curie, c_C) and

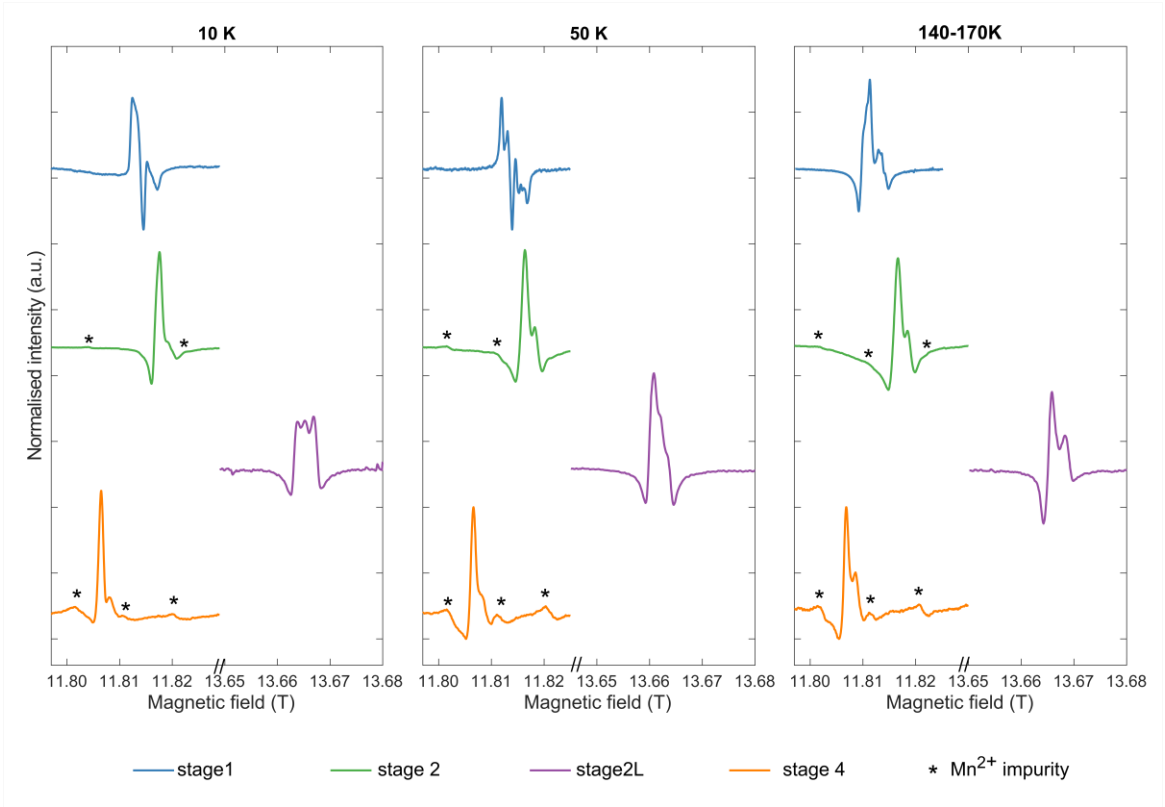

Figure 6. High Frequency EPR spectra of the four lithiation stages of graphite taken at 331 GHz (stages 1, 2, 4) and 383 GHz (stage 2L; purple spectra). Three separate temperature points are presented to show the evolution of the signal with temperature. For the high T spectra, stage 1 was collected at 158 K, stages 2 and 4 at 140 K and stage 2L at 170 K (hence the range given). In the stage 2 and 4 spectra, hyperfine coupling from Mn^{2+} impurities in the capillaries can be observed and are indicated by asterisks (*).

independent components (Pauli, c_P) were extracted from the fit: at 300 K, c_P = 8.4×10^{-5} emu K mol^{-1} and c_C = 3.6×10^{-5} emu K mol^{-1}. Thus, Pauli paramagnetism dominates over Curie paramagnetism, as anticipated for a metallic system with negligible exchange interactions. The Curie contribution corresponds to 0.3 μ_B (Bohr magneton) per LiC_6 unit.[53]

HFEPR. HFEPR was used to investigate the local structure in lithiated graphite anodes. Firstly, we note that all resonances observed here are due to spins on the lithiated graphite and not on any C additives: the resonances corresponding to pristine graphite or Super P Carbon could not be observed at this field. We tentatively attribute this to very fast relaxation of the defect spins in these materials at such high fields.

HFEPR spectra were recorded for all samples at temperatures between 170 K and 10 K (Figure 6) and frequencies between 331 GHz and 441 GHz. The spectra recorded at 50 K showed the highest resolution across all samples, this being most pronounced for the stage 1 sample. This is consistent with the T_{1e} measurements obtained at lower fields where the stage 1 compound showed the longest T_{1e} at 50 – 100K. Surprisingly, the spectra obtained from stages 1 and 2 could not be fit well unless Li hyperfine couplings were included in the simulations. The fits for the dense and dilute stages are presented in Figure 7, respectively, and the fitted *g*-tensors, hyperfine couplings and weights of the different components are given in Table 1.

The 50 K spectrum at 331 GHz for stage 1 was fitted to three different axial systems, accounting for three distinct electron environments (Figure 7(a)); this model was verified by a fit to a spectrum at the same temperature but higher microwave frequency (441 GHz, Figure S13). The first environment (approx. 56% of the overall weight) with g_{iso} = 2.0041, was modelled with isotropic hyperfine couplings of 4.8 MHz to two Li nuclei; we therefore attribute this resonance to electrons in the graphite layers with Li^+ above and below the layer. The second resonance (approx. 31% of the total weight) at g_{iso} = 2.0042 shows

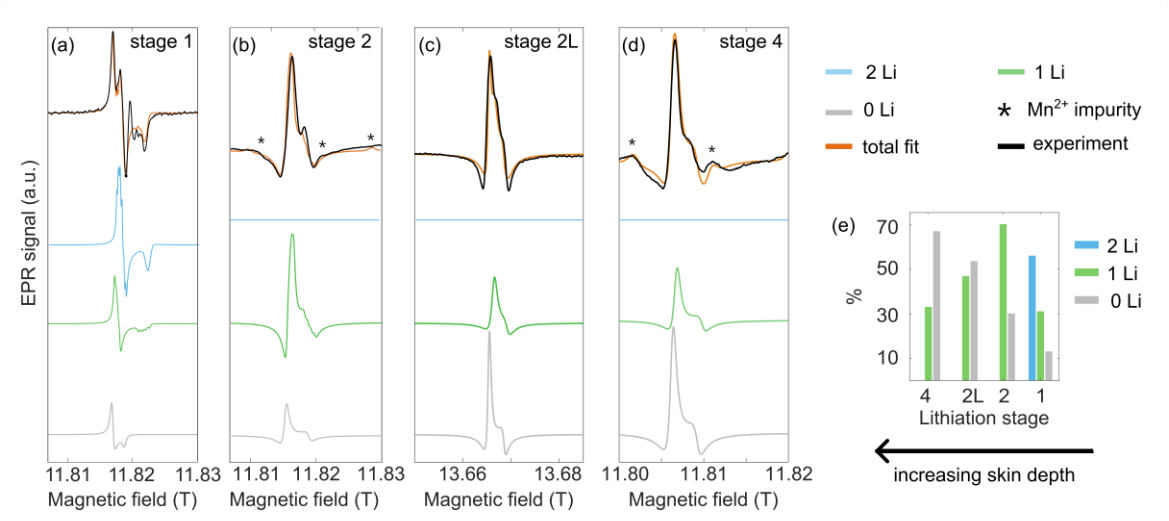

Figure 7. High Frequency EPR spectra of stage 1 (a), stage 2 (b), stage 2L (c) and stage 4 (d) graphite taken at 331 GHz (stages 1, 2, 4) and 383 GHz (stage 2L) at 50 K. The spectrum for stage 1 was fitted to three different axial components, while the spectra of the remaining stages were fitted to two axial components, as outlined in the main text. In the stage 2 and 4 spectra, peaks from Mn^{2+} impurities in the Quartz capillaries are indicated by asterisks. (e) Weight percentage of the different components obtained from fitting HFEPR spectra for the four different lithiation stages at 50 K and 331 GHz (stages 1, 2, 4) and 383 GHz (stage 2L).

hyperfine coupling to only one Li nucleus, A_{iso} = 4.6 MHz, which we attribute to an electron on a graphite sheet with only one Li^+ above or below it—i.e., a stage 2-like environment. Finally, the third axial environment (approx. 13% of the total weight), g_{iso} = 2.0044, shows no hyperfine coupling to Li. We therefore tentatively attribute this resonance spins near defects: spins on or near the surface, perhaps from or near protonated and/or oxygenated C centres (C–H units, hydroxyls, hydrogen-carbonates), or trapped spins at C vacancies, or simply from electrons in graphitic sheets that are either not near Li or where electron-nuclear self-decoupling has occurred (see below).

The spectra for stage 2 can be fitted to two environments, one with an electron coupling to one Li centre and one that couples to no Li centres, with comparable *g*-anisotropy and hyperfine splitting (see Table 1). The relative weights of the two components are approximately 70% for the 1 Li component and 30% for the 0 Li (defect) component. The line-shapes appear phase-shifted in stage 2 compared to stage 1, which we ascribe to the greater conductivity of this phase at T < 200 K (Figure 4(b))—we show in the SI how by phase-shifting the stage 1 spectrum we can achieve similar line-shapes (Figure S14). The spectra appear broader than in stage 1, which is likely a result of the shorter T_{1e} in stage 2 as measured by PEPR (44% shorter compared to stage 1 at 50 K).

In the dilute stages, only the 1 Li component and 0 Li species are present, consistent with the expected layer stackings (Figure 7(c, d)). The relative concentrations of the three environments are compared in Figure 7(e), the 0 Li component becoming more dominant as the Li^+ concentration decreases. We note that across the four stages these weights are not fully quantitative due to skin effects, but we believe they are sufficiently bulk sensitive to be meaningful (see SI for further discussion on the effect of skin depth on the fitting, Figure S15 and S16).

In our simulations we included both Li isotopes (^{6}Li and ^{7}Li) at natural abundance. Additional spectra fitted exclusively with either ^{6}Li or ^{7}Li are shown in the SI (Figure S10 (a,b)). Furthermore, we considered the possibility of there being hyperfine coupling to protons present as impurities in the graphite (e.g., at the edges of the graphene sheets) or possibly on the surfaces of the graphite in the solid-electrolyte interphase (SEI) formed upon electrolyte degradation (Figure S10 (c-e)). The reader is referred to

Table 1. Axial *g*-tensor components for the different phases deduced from fitting the HFEPR spectra of the 4 lithiation stages at 331 GHz (stages 1, 2, 4) and 383 GHz (stage 2L) at 50 K; isotropic *g* recorded at X-band; isotropic *g* as reported by Lauginie and coworkers; hyperfine coupling constant obtained from fitting the HFEPR spectra (in square brackets for the *x, y, z* components). For a complete error analysis of fits to high frequency spectra, refer to SI, section 19.

Stage	2 Li component			1 Li component			0 Li component			*g* (X band, 100 K)	*g* (Lauginie *et al.*)[38]	*A* / MHz
	$g_{x,y}$	g_z	%	$g_{x,y}$	g_z	%	$g_{x,y}$	g_z	%			
1	2.0043	2.0036	56	2.0044	2.0037	31	2.0045	2.0042	13	2.0133	2.0020	[5.0 5.0 4.4] (2Li) [0.2 0.2 13.5] (1 Li)
2	-	-	-	2.0038	2.0033	70	2.0039	2.0034	30	2.0134	2.0022	[0.2 0.2 13.5]
2L	-	-	-	2.0043	2.0038	47	2.0045	2.0039	53	2.0138	2.0026	[2.5 2.5 1.0]
4	-	-	-	2.0054	2.0046	33	2.0054	2.0049	67	2.0145	-	[2.0 2.0 1.0]

the SI for a full discussion. While we cannot rule out the possibility that a small subset of the unpaired electrons are coupled to protons, proton hyperfine coupling is not visible in the spectra of the dilute stages where these protons will also be present. Thus, while somewhat unexpected, we were unable to fit the high field spectra of the stage 1 and 2 samples unless Li hyperfine couplings were included.

The fitted *g*-tensors reproduce the trend seen in the X-band data across stages (Table 1), where a greater contribution of the Li band to the Fermi level results in *g*-tensor components closer to g_e. We note that the components of the *g*-tensors are in general closer to g_e at high frequency than they are at X-band. This is tentatively ascribed to non-linear Zeeman splitting at such high fields and to the decoupling of the SOC component from the electron spin (Paschen-Back effect).[54,55]

Discussion.

The effect of electrical conductivity on EPR parameters and electronic properties. The electronic properties of lithiated graphite depend on the nature of the electrons nearest the Fermi level, which are strongly influenced by local and long-range structure; these in turn dictate its electrochemical performance.

Local electronic structure of Li-intercalated graphite.

Li 2s Contribution to Fermi Level. The *g*-factors are a probe of the density of states at the Fermi level in Li-intercalated graphite. As shown above in Figure 4(a), the *g*-tensors at both X-band and high frequencies shift towards g_e from pristine graphite to fully lithiated (stage 1) graphite. As Li intercalates between the graphite sheets, electrons are introduced in the graphite conduction band and graphite is reduced, the contribution of Li 2s orbitals at the Fermi level increasing. The primary consequence of this is a reduction in the SOC component of the *g*-tensors, resulting in the observed shift towards g_e. This trend had been previously reported in the literature (albeit with slightly different *g*-values, reported for convenience in Table 1) by Lauginie and coworkers,[42] who showed a similar decrease across the first three stages as Li concentration increased.

Local structure from HFEPR. While X-band EPR provided information on the bulk metallic properties of Li-intercalated graphite, HFEPR allowed us to investigate more closely the local electronic structure of these materials.

The high-frequency spectra (Figure 7(a-d)) can be fitted to 3 components (stage 1) and 2 components (stages 2, 2L, 4), with two of these components (2 Li and 1 Li) showing hyperfine coupling to Li (Table 1). We note that while hyperfine splittings are often more easily resolved at lower frequencies, where *g*-anisotropy and *g*-strain are less pronounced, they have occasionally been observed at high frequency in *e.g.* glass matrices.[56,57] In our case, the higher fields allow the principal components of the g tensor, $g_{x,y}$ and g_z to be resolved, in principle, making it easier to resolve an anisotropic hyperfine coupling constants. This is illustrated via simulations in the SI of the X-band spectra (Figure S12). The presence of three different environments in stage 1 is not surprising considering the difficulty in isolating pure stage 1 electrochemically.[51] The isotropic hyperfine coupling constants for the two Li (stage 1) components and one Li (stage 2) component in the HFEPR fits are 4.8 MHz and between 3-5 MHz, respectively (for a full error analysis, refer to SI, section 19). The larger principal component of the hyperfine tensor in the 1 Li environment (A_z = 13.5 MHz) is assigned, at least in part, to a change in the interlayer spacing (it increases from stage 2 to stage 1).[58] This

difference results in a change to the overlap of Li^+ orbitals and carbon-based orbitals near the Fermi level. Additionally, we note that in a stage 2-type Li environment, the electron is shared between the carbon layers above and below; in a stage 1 compound, while this is still the case, the carbon layers also are bound to 1 Li above and below the carbon layers. I.e., the electron is shared over two Li ions. Thus, intuitively, the contribution of the Li 2s orbital to primarily 2p carbon band will be larger.

These hyperfine coupling constants can be compared with the ^{7}Li NMR Knight shifts (see Figure S2), where stage 2 has a larger shift (45.0 ppm) compared to stage 1 (42.6 ppm), also suggesting a greater population of the Li 2s orbitals at the Fermi level for stage 2.[13] The NMR Knight shift (δ_{KS}) can be correlated to the isotropic hyperfine coupling constant, A_{iso}, through the following equation:[28,59]

$$A_{\mathrm{iso}} = \frac{\delta_{KS} N_{\mathrm{A}} \mu_0 \mu_{\mathrm{N}} \mu_{\mathrm{B}} g_{\mathrm{e}} g_{\mathrm{N}}}{\chi_M \, h * 10^6} \qquad (6)$$

where N_A is Avogadro's constant, μ_0 is the vacuum permeability, μ_N is the nuclear magneton, and g_N is the nuclear *g*-factor, χ_M is the molar susceptibility (cf. Figure S9) at 50 K (the temperature of the HFEPR spectrum) and *h* is Planck's constant. Using Eqn.(6) and the experimental NMR shifts, we calculate A_{iso} = 4.6 MHz for stage 1 and A_{iso} = 3.4 MHz for stage 2. While further EPR experiments with, for example, samples containing ^{6}Li only, or with different concentrations of defects, will help us test alternative hypotheses, it is remarkable that the fitted EPR spectra and NMR Knight shifts and measured susceptibilities result in hyperfine constants of the same order of magnitude.

These hyperfine coupling constants should be contrasted with the much larger isotropic hyperfine coupling constant of A_{iso} = 52.7 MHz for Li metal, calculated here using the ^{6,7}Li Knight Shift, δ_{KS}, of 245 ppm and susceptibility, χ_M of 1.99×10^{-10} m^3 mol^{-1}[60]. Hence, the hyperfine coupling constants for lithiated graphite, like the NMR shifts, confirm that the Li ions are partially charged and not present as Li^0. If the additional electrons inserted into the conduction band associated with the Li intercalation had all been located on the Li ions, much larger hyperfine couplings would be expected.

Finally, we note that the hyperfine coupling constant extracted by EPR reflects an admixture of both Fermi-Contact and dipolar components due to electron-nuclear dipolar interactions not being averaged e.g. by spinning in NMR, accounting for the large anisotropy in *A*. On the other hand, the hyperfine shift obtained through MAS NMR is solely due to the Fermi-Contact shift, as the dipolar interaction is averaged out.

Finally, we should consider the question of why hyperfine coupling constants are seen despite the very rapid mobility of electrons, which diffuse over very long distances on the timescale of the hyperfine interaction.[32] We note here that we see both a Curie and Pauli contribution to the magnetism (i.e., a temperature dependent and temperature independent term). One possibility is that in these disordered graphites a subset of the electrons in the carbon sheets are similarly partially localised nearby defects, contributing to the Curie component and resulting in observable Li hyperfine coupling constants if the Li ions are near these defects. However, it should be noted that when hard carbons, which contain highly disordered graphene sheets, are lithiated (or sodiated), sites near the defects are lithiated (sodiated) first, i.e., at higher voltages,[61] which means we might expect to see this phenomenon at higher states of charge, not just in the stage 1 and 2 compound. A study of single graphene sheets has discussed the role that defects

(non-bonding orbitals, NBOs) play in controlling EPR spectra and magnetic susceptibility proposing that the role of NBOs will depend strongly on the degree of hole or electron doping in the graphene sheets.[62] Future high field EPR studies will focus on different graphites with differing degrees of disorder/particle sizes and potentially with different degrees of isotopic enrichment.

Metallicity. X-band EPR spectra can provide (semi)-quantitative information about metallicity of lithiated graphite through the *A/B* ratios and electron relaxation times.

The electrical conductivity of the graphite intercalation materials is affected by the following factors: carrier concentration, electron hopping between defects states (from defects or dopants), which is thermally activated, and the presence of phonons, both which reduce the electron mean-free path, scattering the electrons and increasing the resistivity.[5] Unlike pristine graphite, where temperature plays a substantial role in carrier generation, lithiated graphite is expected to have a larger temperature-independent carrier concentration due to the larger density of states at the Fermi level within the conduction band. Graphite's layered, anisotropic structure results in different in-plane and out-of-plane conductivities, the *a/c* conductivity ratio decreasing substantially upon lithiation, as discussed above.

In EPR, the metallic character of lithiated graphite, and therefore the presence of skin effects, results in $A/B > 1$. The *A/B* parameter depends on the conductivity and the EPR frequency (equation (3)), less conductive samples and/or low microwave frequencies increasing the skin depth and therefore the number of electrons probed by EPR. *A*/*B* also depends on the size of particles and their packing density, as this also affects the ability of the microwaves to penetrate into the sample.[32] This phenomenon was clearly observed for stage 1 packed loosely in a capillary vs a rotor (Figure S8) where *A/B* ratios of 1.96 and 3.8, respectively, were seen. Since all the samples were made from the same pristine graphite sample, and assuming similar packing, the *A/B* ratio is a probe of relative conductivity between samples and its temperature dependence. As shown in Figure 4(b), the dense stages (1 and 2) have a larger *A/B* ratio than the dilute stages (2L and 4) across all temperatures. The *A/B* ratio increases as temperature is lowered for all stages, indicating increasing conductivity. However, the rate of change in the *A/B* ratio is smaller for stage 1, indicating that it is a better metal. In intercalation compounds involving heavier alkali metals, the change in resistivity, ρ, has been fit with a function of the form, $\rho = a + bT + cT^2$, the terms linear in T and T^2 being ascribed to phonon-electron and electron-electron scattering processes, respectively, both processes increasing as the temperature is increased.[5,6] Given that the *A/B* ratio depends on the d/δ, and that δ is proportional to $\sigma^{-1/2}$ (equation(3)), and thus $\rho^{1/2}$, a strong dependence of the *A/B* ratio on temperature might similarly be expected. Attempts to fit the *A/B* ratio using a temperature dependence of a form used to describe $\rho^{-1/2}$ were not, however, successful, the *A/B* ratio becoming less (rather than more) dependent on temperature closer to room temperature. This is shown in the SI where the *A/B* ratio was fitted to two close-to-linear regimes, above 200 K and below 200 K for stage 2 and approximately 210 K for stages 2L and 4 (see Figure S17 and Table S4) to illustrate the reduced temperature dependence at higher temperatures. This phenomenon may be simply due to the fact that at above approximately 210 K the skin depth δ starts to approach the sample thickness, d, the regime where the *A/B* ratio is less sensitive to any changes in δ.

It should be noted that the skin depth was estimated above without taking in account any anisotropy in the conductivity. While there is some scatter in the data, likely because of the difficulty in synthesising fully lithiated (pure-phase) LiC_6, conductivities in the *ab* plane of 2.4 $\times 10^5$ S cm^{-1} at room temperature have been measured (increasing by about a factor of 5 at 100K), while the conductivity at room temperature in the perpendicular (*c*-) direction is about 14 times lower.[6,63] If we consider that the surface areas of most polycrystalline graphites (including that used here, see Figure S1) is dominated by the *ab* basal planes, then the skin depth perpendicular to the *ab* planes is actually 4 μm at room temperature (cf. 1 μm parallel to the planes) and indeed of the order of many of the particles' radii; thus X-band microwaves can penetrate through the graphite basal planes deep into the bulk of the samples at room temperature. However, a factor of five increase in basal plane conductivities has been observed on lowering the temperature to 100 K in stage-1 and 2 Li compounds, and thus skin depths will be more pronounced at lower temperatures. Increased overlap between the carbon layers (associated with the contraction seen in the *c*-direction, particularly in the lower stages), should similarly be associated with a higher conductivity.

The measured values for the *A/B* ratio close to 2 are consistent with *d* and *δ* values of the same order of magnitude (independent of the theory and assumptions about sample geometry used to derive expressions for *A/B* vs d/*δ*).[32] Using a skin depth of 4 μm and an average particle diameter of 13 μm produces a *d/δ* ratio of approximately 3.25 for stage 1 (at room temperature) and (from Figure 15 in ref[32]) an estimated *A/B* ratio of approximately 2, consistent with the value measured here.

Electron relaxation times. The effect of metallicity is also observed in the electron relaxation times. Two main phenomena affect T_{1e} and T_{2e}: skin effects and collisions with defects. Both phenomena are influenced by electron mobility.

The T_{1e} (measured by pulsed EPR) track the T_{2e} (determined from the X-band linewidth), but are approximately 2-3 times shorter (the effect is more pronounced for stages 1 and 2 vs 2L or 4, see SI Table S5). This likely reflects how the T_{1e} is measured: either a saturation or 180º pulse is first applied, during which the electrons move in and out of the skin depth region, feeling the effect of the pulse at random intervals and with varying power levels.

One relevant parameter is T_D, the time to move out of the skin depth region. Assuming 1D diffusion in the *c*-direction is the most relevant, then using the values for LiC_6 of the electron diffusivity, *D*, in the *c*-direction of 18 cm^2 s^{-1} (from Lauginie *et al.*)[42] and the skin depth in the c-direction δ = 4 μm (from *c*-conductivity at RT) then from equation (5) T_D in the c-direction is approximately 2 ns. This is much shorter than the 16 ns 180-degree pulse used in the inversion recovery experiment and a tip angle of 180 will not be achieved, particularly for large particles. Furthermore, the resonances of all stages are also too broad to be effectively excited. Thus, the induced magnetisation will take a shorter time to return to equilibrium following the pulse and the measured T_{1e} is shorter than the true value. Similarly, a long saturation pulse will likely not completely saturate the signal again because the resonance is too broad and because of skin depth issues (some residual magnetisation remains and a shorter time is required to reach equilibrium). Thus, it is perhaps more appropriate to refer to these measured T_{1e}s as effective or scaled T_{1e}s or T_{1e}*. Despite the challenges in measuring the T_{1e}, T_{2e}, as measured from the linewidth, will contain contributions from the *g*-anisotropy, hence it still useful to consider the T_{1e}* values.

The T_{1e} (and T_{2e}) are affected by the mean free path *a* before a collision with defects, and also the probability that a collision will lead to a change of spin, together quantified *via* the spin depth. There are two types of defects, extrinsic dopants/defects and those caused by interactions with lattice phonon modes. In general, the SOC decreases with increasing lithium content, the SOC helping to drive spin flips. Consistent with this, Lauginie et al. observed that the T_{2e} values (as determined from the linewidth) of stage 1 and stage 2 graphite compounds decreased with increasing atomic number of the intercalant atom (from Li – Rb), consistent with the SOC mechanism.[42] This mechanism is also consistent with our generally longer T_{1e}* (and T_{2e}) values for stage 1 and is consistent with its small *g*-values (which again indicate smaller SOC): Elliot showed that the T_{2e} was proportional to $T_R/(\Delta g)^2$, where T_R represents the time between collisions (a function of the electron diffusivity and mean free path, *a*), and Δg the deviation from g_e. The shorter T_{1e}s of the higher stages correlate to a degree to the greater carbon $2p_z$ contribution to density of states at the Fermi Level.

With decreasing temperature, the time between collisions with phonons increases, and we would expect the T_{1e}* to lengthen. This trend is observed for stages 1 and 2 (down to 100K) but not for the less dense stages. Instead, for stages 2L and 4, T_{1e}^* gradually decreases with temperature. The two different trends for the T_{1e}s of the dilute and dense stages suggest that metallicity plays a more significant role in electron relaxation of stages 1 and 2. Furthermore, stages 1 and 2 have greater three-dimensional conductivity due to the Li^+ sitting between the graphite layers.

The T_{1e}s decrease below approximately 100 K in stage 1 and 2. This turnover in the dense stages correlates with the magnetometry data, where antiferromagnetic ordering at 15 K and 25 K was seen for stages 1 and 2, respectively (see Figure S9). The magnetic response can be divided into a Curie and temperature-independent (Pauli) component; on cooling, the electron spin fluctuations will diminish as the thermal energy decreases and eventually their magnitude is no longer sufficient to overcome the local exchange constants, likely resulting in the development of (some) locally ordered spin clusters, reducing the Curie component of the susceptibility. Rapid motion of the electrons results in collisions with these localised spins/clusters and an additional mechanism for reducing the T_{1e}, when the local fluctuations of these clusters enter the T_{1e} timescale (the X-band Larmor frequency).[42,43,64] As a result, the relaxation times initially increase with decreasing temperature (due to fewer phonon scattering effects) and then decrease at low temperatures, due to magnetic exchange effects; a maximum in T_{1e} is therefore seen for these samples.

In contrast, no turnover in T_{1e} is seen for the dilute stages, suggesting an absence of (significant) exchange coupling effects, consistent with the lower electron spin concentration at these lower lithiation levels; this is consistent with their much lower zero-field-cooled (ZFC) susceptibilities (see Figure S9).

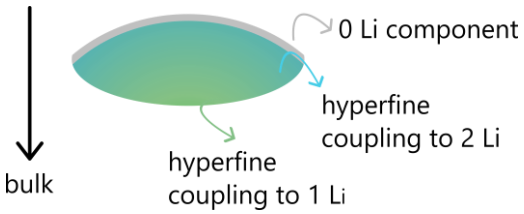

Figure 8. Visualisation of the Li concentration gradient in a stage 1 particle based on weights of the different components of the fit as reported in Figure 7(e).

Local structure and skin effects. An important consequence of the metallicity of charged graphite is the presence of skin

effects, which determine the relative weights of the different environments that are observed especially at higher frequency and low temperature, where the skin depth is significantly reduced (Eqn. (3), δ is ~0.5 and 0.7 μm at 331 GHz and 300 K for the skin depth in the ab- and c-directions). Analysis of the effect of skin depth on HFEPR spectra taken at 10 K, 15 K and 50 K (Figure S15 and S16) provides a spatial map of the different components, with the defect spins being at or closer to the surface (since the weight of this component remained constant across the three temperature points examined here, the skin depth decreasing as temperature is decreased and conductivity increases), followed by the 2 Li component, and with the 1 Li component towards the core. This suggests that lithiation is associated with a concentration gradient, with the core being less lithiated than the shell of the particle (Figure 8). Thus HFEPR probes the heterogeneity in lithiation, the results indicating that it is difficult to fully lithiate the centre of the particle. The presence of both the 1Li and 2Li environments in the stage 1 sample, the 1Li environment having a different *g*-factor than that seen for the stage 2 material suggests that the 1Li environment is different in the two materials and affected by the presence of 2Li environments. This suggests that at least some of these 1Li environments in the stage 1 compound are present as stacking faults and thus in close proximity to the 2Li environments.

Conclusions

In this work we aimed to increase our understanding of the electronic structure of Li-intercalated graphite at different stages, namely dense stages 1 and 2, and dilute stages 2L and 4 by using a variety of EPR methods. Electrochemical cycling and ^{7}Li NMR were also used to assess phase purity as well as to contextualise the results in the battery domain.

Variable temperature X-band EPR was sensitive to the degree of metallicity of the four different stages, with the temperature-dependence of the *A/B* ratios indicating a greater electrical conductivity and more significant skin effects at low temperatures across all stages. The dense stages showed more metallic behaviour than the dilute stages, the A/B ratio increasing with decreasing temperature consistent with higher conductivities. The metallic character introduced by Li intercalation is also reflected in the observed *g*-factors, where the greater contribution of the Li 2*s* band to the density of states at the Fermi level is responsible for the shift in the measured *g*-factors towards g_e on lithiation.

X-band Pulsed EPR was used to estimate the longitudinal electron relaxation times, T_{1e}s, which show different temperature dependence for the dilute and dense stages and which were explained in terms of the effect of phonons/defects on scattering processes and the magnetic properties of the samples.

The measured T_{1e}s are also fundamental in assessing optimal conditions for Dynamic Nuclear Polarisation (DNP) NMR experiments, where the electron polarisation is transferred to nearby nuclei enhancing their NMR signal. The longest T_{1e}s are seen for stage 1 compounds at around 100K.

Finally, HFEPR showed the presence of hyperfine coupling between the metallic electrons and ^{7}Li observed here for the first time, the values indicating that the electrons in lithiated graphite largely occupy carbon-based orbitals. HFEPR showed that the electrochemically isolated stage 1 sample also contained stage-2 like local environments, indicating the presence of graphitic interlayers containing no Li. The relative weight of these two components changed as a function of temperature due to changes in conductivity and thus skin-depth effects, indicating that more stage 2

environments are present in the bulk of the particles, reflecting the difficulty in fully lithiating graphite. Further studies are, however, required to understand the role that delocalised (metallic) and more localised spins/clusters play in giving rise to the observed electron-lithium hyperfine couplings observed at high fields.

Our work demonstrates the power of EPR spectroscopy in investigating the local electronic structure of graphite on cycling, paving the way for this technique as a tool for investigating the electronic properties of novel materials for use in lithium-ion batteries. This work also sets out a framework for screening materials for DNP, a tool for selective excitation of species near surfaces (for example the solid-electrolyte interphase)[65,66] and/or paramagnetic centres (for example in the bulk of cathodes and solid electrolytes).[67,68]

AUTHOR INFORMATION

Corresponding Author

*E-mail: cpg27@cam.ac.uk

ORCID

Teresa Insinna: 0000-0001-6484-4323

Euan N. Bassey: 0000-0001-8827-7175

Katharina Märker: 0000-0002-5056-7174

Clare P. Grey: 0000-0001-5572-192X

Notes

There are no conflicts of interest to declare.

Supporting Information

The Supporting Information, containing the solid state NMR spectra, additional High Frequency parameters and data, magnetometry data and additional fits to the X-band and High Frequency spectra is available free of charge on … at DOI:

ACKNOWLEDGEMENTS

T.I. and C.P.G. were supported by an ERC Advanced Investigator Grant for C.P.G. (EC H2020 835073). E.N.B. was supported by the Engineering Physical Sciences Research Council (EPSRC) via the National Productivity Interest Fund (NPIF) 2018. K.M. was supported by the Faraday Institution Degradation Project (FIRG001 and FIRG024). The Pulsed EPR measurements were performed at the Centre for Pulse EPR at Imperial College London (PEPR), supported by the EPSRC grant EP/T031425/1.

Dr D. Maxwell and Prof. H. Sirringhaus are gratefully acknowledged for helpful discussions.

References:

(1) Goodenough, J. B.; Park, K.-S. The Li-Ion Rechargeable Battery: A Perspective. *J. Am. Chem. Soc.* **2013**, *135* (4), 1167–1176. https://doi.org/10.1021/ja3091438.

(2) Asenbauer, J.; Eisenmann, T.; Kuenzel, M.; Kazzazi, A.; Chen, Z.; Bresser, D. The Success Story of Graphite as a Lithium-Ion Anode Material – Fundamentals, Remaining Challenges, and Recent Developments Including Silicon (Oxide) Composites. *Sustainable Energy & Fuels* **2020**, *4* (11), 5387–5416. https://doi.org/10.1039/D0SE00175A.

(3) Nitta, N.; Wu, F.; Lee, J. T.; Yushin, G. Li-Ion Battery Materials: Present and Future. *Materials Today* **2015**, *18* (5), 252–264. https://doi.org/10.1016/j.mattod.2014.10.040.

(4) Kaskhedikar, N. A.; Maier, J. Lithium Storage in Carbon Nanostructures. *Advanced Materials* **2009**, *21* (25–26), 2664–2680. https://doi.org/10.1002/adma.200901079.

(5) Dresselhaus, M. S.; Dresselhaus, G. Intercalation Compounds of Graphite. *Advances in Physics* **1981**,

30 (2), 139–326. https://doi.org/10.1080/00018738100101367.

(6) Basu, S.; Zeller, C.; Flanders, P. J.; Fuerst, C. D.; Johnson, W. D.; Fischer, J. E. Synthesis and Properties of Lithium-Graphite Intercalation Compounds. *Materials Science and Engineering* **1979**, *38* (3), 275–283. https://doi.org/10.1016/0025-5416(79)90132-0.

(7) Fischer, J. E. Electronic Properties of Graphite Intercalation Compounds. *Materials Science and Engineering* **1977**, *31*, 211–223. https://doi.org/10.1016/0025-5416(77)90037-4.

(8) Billaud, D.; McRae, E.; Hérold, A. Synthesis and Electrical Resistivity of Lithium-Pyrographite Intercalation Compounds (Stages I, II and III). *Materials Research Bulletin* **1979**, *14* (7), 857–864. https://doi.org/10.1016/0025-5408(79)90149-1.

(9) Guerard, D.; Herold, A. Intercalation of Lithium into Graphite and Other Carbons. *Carbon* **1975**, *13* (4), 337–345. https://doi.org/10.1016/0008-6223(75)90040-8.

(10) Daumas, N.; Hérold, A. Relations entre la notion de stade et les mécanismes réactionnels dans les composés d'insertion du graphite. *C R Acad Sc Paris* **1969**, *268*, 373.

(11) Rüdorff, W.; Hofmann, U. Über Graphitsalze. *Zeitschrift für anorganische und allgemeine Chemie* **1938**, *238* (1), 1–50. https://doi.org/10.1002/zaac.19382380102.

(12) Dahn, J. R. Phase Diagram of LiC6. *Phys. Rev. B* **1991**, *44* (17), 9170–9177. https://doi.org/10.1103/PhysRevB.44.9170.

(13) Letellier, M.; Chevallier, F.; Morcrette, M. In Situ 7Li Nuclear Magnetic Resonance Observation of the Electrochemical Intercalation of Lithium in Graphite; 1st Cycle. *Carbon* **2007**, *45* (5), 1025–1034. https://doi.org/10.1016/j.carbon.2006.12.018.

(14) Chevallier, F.; Poli, F.; Montigny, B.; Letellier, M. In Situ7Li Nuclear Magnetic Resonance Observation of the Electrochemical Intercalation of Lithium in Graphite: Second Cycle Analysis. *Carbon* **2013**, *61*, 140–153. https://doi.org/10.1016/j.carbon.2013.04.078.

(15) Didier, C.; Pang, W. K.; Guo, Z.; Schmid, S.; Peterson, V. K. Phase Evolution and Intermittent Disorder in Electrochemically Lithiated Graphite Determined Using in Operando Neutron Diffraction. *Chem. Mater.* **2020**, *32* (6), 2518–2531. https://doi.org/10.1021/acs.chemmater.9b05145.

(16) Ohzuku, T.; Iwakoshi, Y.; Sawai, K. Formation of Lithium-Graphite Intercalation Compounds in Nonaqueous Electrolytes and Their Application as a Negative Electrode for a Lithium Ion (Shuttlecock) Cell. *J. Electrochem. Soc.* **1993**, *140* (9), 2490. https://doi.org/10.1149/1.2220849.

(17) Allart, D.; Montaru, M.; Gualous, H. Model of Lithium Intercalation into Graphite by Potentiometric Analysis with Equilibrium and Entropy Change Curves of Graphite Electrode. *J. Electrochem. Soc.* **2018**, *165* (2), A380–A387. https://doi.org/10.1149/2.1251802jes.

(18) Boesenberg, U.; Sokaras, D.; Nordlund, D.; Weng, T.-C.; Gorelov, E.; Richardson, T. J.; Kostecki, R.; Cabana, J. Electronic Structure Changes upon Lithium Intercalation into Graphite – Insights from Ex Situ and Operando x-Ray Raman Spectroscopy. *Carbon* **2019**, *143*, 371–377. https://doi.org/10.1016/j.carbon.2018.11.031.

(19) Shu, Z. X.; McMillan, R. S.; Murray, J. J. Electrochemical Intercalation of Lithium into Graphite. *J.*

Electrochem. Soc. 1993, *140* (4), 922–927. https://doi.org/10.1149/1.2056228.

(20) Mukai, K.; Inoue, T. Magnetic Susceptibility Measurements on Li-Intercalated Graphite: Paramagnetic to Diamagnetic Transitions in C12Li Induced by Magnetic Field. *Carbon* 2017, *123*, 645–650. https://doi.org/10.1016/j.carbon.2017.08.012.

(21) Wandt, J.; Marino, C.; Gasteiger, H. A.; Jakes, P.; Eichel, R.-A.; Granwehr, J. Operando Electron Paramagnetic Resonance Spectroscopy – Formation of Mossy Lithium on Lithium Anodes during Charge–Discharge Cycling. *Energy Environ. Sci.* 2015, *8* (4), 1358–1367. https://doi.org/10.1039/C4EE02730B.

(22) Dutoit, C.-E.; Tang, M.; Gourier, D.; Tarascon, J.-M.; Vezin, H.; Salager, E. Monitoring Metallic Sub-Micrometric Lithium Structures in Li-Ion Batteries by in Situ Electron Paramagnetic Resonance Correlated Spectroscopy and Imaging. *Nat Commun* 2021, *12* (1), 1410. https://doi.org/10.1038/s41467-021-21598-2.

(23) Nguyen, H.; Clément, R. J. Rechargeable Batteries from the Perspective of the Electron Spin. *ACS Energy Lett.* 2020, *5* (12), 3848–3859. https://doi.org/10.1021/acsenergylett.0c02074.

(24) See, K. A.; Lumley, M. A.; Stucky, G. D.; Grey, C. P.; Seshadri, R. Reversible Capacity of Conductive Carbon Additives at Low Potentials: Caveats for Testing Alternative Anode Materials for Li-Ion Batteries. *J. Electrochem. Soc.* 2016, *164* (2), A327. https://doi.org/10.1149/2.0971702jes.

(25) Hong, J. K.; Lee, J. H.; Oh, S. M. Effect of Carbon Additive on Electrochemical Performance of LiCoO2 Composite Cathodes. *Journal of Power Sources* 2002, *111* (1), 90–96. https://doi.org/10.1016/S0378-7753(02)00264-1.

(26) Dyson, F. J. Electron Spin Resonance Absorption in Metals. II. Theory of Electron Diffusion and the Skin Effect. *Phys. Rev.* 1955, *98* (2), 349–359. https://doi.org/10.1103/PhysRev.98.349.

(27) Feher, G.; Kip, A. F. Electron Spin Resonance Absorption in Metals. I. Experimental. *Phys. Rev.* 1955, *98* (2), 337–348. https://doi.org/10.1103/PhysRev.98.337.

(28) Pell, A. J.; Pintacuda, G.; Grey, C. P. Paramagnetic NMR in Solution and the Solid State. *Progress in Nuclear Magnetic Resonance Spectroscopy* 2019, *111*, 1–271. https://doi.org/10.1016/j.pnmrs.2018.05.001.

(29) Atkins, P. K.; Friedman, R. S. *Molecular Quantum Mechanics*, Third Edition.; Oxford University Press, 1997.

(30) Weil, J. A.; Bolton, J. R. *Electron Paramagnetic Resonance: Elementary Theory and Practical Applications*, 2nd ed.; Wiley-Interscience: Hoboken, N.J, 2007.

(31) Yafet, Y. G Factors and Spin-Lattice Relaxation of Conduction Electrons**Part of the Work Connected with the Preparation of This Article, in Particular the Work on Spin-Lattice Relaxation, Was Done While the Author Was at the Westinghouse Research Laboratories, Pittsburgh, Pennsylvania. In *Solid State Physics*; Seitz, F., Turnbull, D., Eds.; Academic Press, 1963; Vol. 14, pp 1–98. https://doi.org/10.1016/S0081-1947(08)60259-3.

(32) Edmonds, R. N.; Harrison, M. R.; Edwards, P. P. Chapter 9. Conduction Electron Spin Resonance in Metallic Systems. *Annu. Rep.*

Prog. Chem., Sect. C: Phys. Chem. **1985**, *82* (0), 265–308. https://doi.org/10.1039/PC9858200265.

(33) Roessler, M. M.; Salvadori, E. Principles and Applications of EPR Spectroscopy in the Chemical Sciences. *Chem. Soc. Rev.* **2018**, *47* (8), 2534–2553. https://doi.org/10.1039/C6CS00565A.

(34) Pifer, J. H.; Magno, R. Conduction-Electron Spin Resonance in a Lithium Film. *Phys. Rev. B* **1971**, *3* (3), 663–673. https://doi.org/10.1103/PhysRevB.3.663.

(35) Palenskis, V. Drift Mobility, Diffusion Coefficient of Randomly Moving Charge Carriers in Metals and Other Materials with Degenerated Electron Gas. *World Journal of Condensed Matter Physics* **2013**, *3* (1), 73–81. https://doi.org/10.4236/wjcmp.2013.31013.

(36) Castle, J. G. Paramagnetic Resonance Absorption in Graphite. *Phys. Rev.* **1953**, *92* (4), 1063–1063. https://doi.org/10.1103/PhysRev.92.1063.

(37) Wagoner, G. Spin Resonance of Charge Carriers in Graphite. *Phys. Rev.* **1960**, *118* (3), 647–653. https://doi.org/monod.

(38) Singer, L. S.; Wagoner, G. Electron Spin Resonance in Polycrystalline Graphite. *J. Chem. Phys.* **1962**, *37* (8), 1812–1817. https://doi.org/10.1063/1.1733373.

(39) McClure, J. W.; Yafet, Y. THEORY OF THE G-FACTOR OF THE CURRENT CARRIERS IN GRAPHITE SINGLE CRYSTALS. *Proceedings from the fifth carbon conference* **1962**, 22–28.

(40) Pines, D.; Slichter, C. P. Relaxation Times in Magnetic Resonance. *Phys. Rev.* **1955**, *100* (4), 1014–1020. https://doi.org/10.1103/PhysRev.100.1014.

(41) Pfluger, P.; Müller, K. A.; Berlinger, W.; Geiser, V.; Güntherodt, H.-J. Anisotropic Metallic Character of C6Li from CESR. *Synthetic Metals* **1983**, *8* (1), 15–21. https://doi.org/10.1016/0379-6779(83)90004-8.

(42) Lauginie, P.; Estrade, H.; Conard, J.; Guérard, D.; Lagrange, P.; El Makrini, M. Graphite Lamellar Compounds EPR Studies. *Physica B+C* **1980**, *99* (1), 514–520. https://doi.org/10.1016/0378-4363(80)90288-0.

(43) Pfluger, P.; Güntherodt, H.-J. Intercalated Graphite — A Synthetic Metal I. Introduction and Electronic Structure. In *Festkörperprobleme 21*; Treusch, J., Ed.; Advances in Solid State Physics; Springer Berlin Heidelberg: Berlin, Heidelberg, 1981; Vol. 21, pp 271–311. https://doi.org/10.1007/BFb0108608.

(44) Dresselhaus, G. F.; Dresselhaus, M. S.; Mavroides, J. G. Spin-Orbit Interaction in Graphite. *Carbon* **1966**, *4* (3), 433–440. https://doi.org/10.1016/0008-6223(66)90056-X.

(45) Barra, A.-L.; Brunel, L.-C.; Baumann, F.; Schwach, M.; Moscherosch, M.; Kaim, W. High-Frequency (245 GHz) and X-Band EPR Study of Stable Dicopper Radical Complexes. *J. Chem. Soc., Dalton Trans.* **1999**, No. 21, 3855–3857. https://doi.org/10.1039/A903419F.

(46) Barra, A. L.; Brunel, L. C.; Robert, J. B. EPR Spectroscopy at Very High Field. *Chemical Physics Letters* **1990**, *165* (1), 107–109. https://doi.org/10.1016/0009-2614(90)87019-N.

(47) Stoll, S.; Schweiger, A. EasySpin, a Comprehensive Software Package for Spectral Simulation and Analysis in EPR. *Journal of Magnetic Resonance* **2006**, *178* (1), 42–55. https://doi.org/10.1016/j.jmr.2005.08.013.

(48) Henson, R. W.; Reynolds, W. N. Lattice Parameter Changes in Irradiated Graphite. *Carbon* **1965**, *3* (3), 277–287.

https://doi.org/10.1016/0008-6223(65)90062-X.
(49) Stankowski, J.; Waplak, S.; Bednarski, W. The Anisotropy and Temperature Dependence of G-Factor in Graphite. *Solid State Communications* **2000**, *115* (9), 489–491. https://doi.org/10.1016/S0038-1098(00)00208-8.
(50) Steward, E. G.; Cook, B. P.; Kellett, E. A. Dependence on Temperature of the Interlayer Spacing in Carbons of Different Graphitic Perfection. *Nature* **1960**, *187* (4742), 1015–1016. https://doi.org/10.1038/1871015a0.
(51) Maxwell, D. NMR Studies of the Electronic Structure, Lithium-Ion Dynamics, and Prelithiation of Lithium-Ion Battery Anode Materials. Thesis, University of Cambridge, 2022. https://doi.org/10.17863/CAM.85357.
(52) Goldfarb, D.; Stoll, S. *EPR Spectroscopy: Fundamentals and Methods*; eMagRes; Wiley, 2018.
(53) Blundell, S.; Blundell, S. *Magnetism in Condensed Matter*; Oxford Master Series in Physics; Oxford University Press: Oxford, New York, 2001.
(54) Kapitza, P. L.; Strelkov, P. G.; Laurman, E. The Zeeman and Paschen-Back Effects in Strong Magnetic Fields. *Proc. R. Soc. Lond. A* **1938**, *167* (928), 1–15. https://doi.org/10.1098/rspa.1938.0114.
(55) Hori, H.; Miki, M.; Date, M. Paschen-Back Effect of D-Lines in Sodium under a High Magnetic Field. *J. Phys. Soc. Jpn.* **1982**, *51* (5), 1566–1570. https://doi.org/10.1143/JPSJ.51.1566.
(56) Fielding, A. J.; Brodhun, F.; Koch, C.; Pievo, R.; Denysenkov, V.; Feussner, I.; Bennati, M. Multifrequency Electron Paramagnetic Resonance Characterization of PpoA, a CYP450 Fusion Protein That Catalyzes Fatty Acid Dioxygenation. *J. Am. Chem. Soc.* **2011**, *133* (23), 9052–9062. https://doi.org/10.1021/ja202207t.
(57) Gerfen, G. J.; Bellew, B. F.; Un, S.; Bollinger, J. M.; Stubbe, J.; Griffin, R. G.; Singel, D. J. High-Frequency (139.5 GHz) EPR Spectroscopy of the Tyrosyl Radical in Escherichia Coli Ribonucleotide Reductase. *J. Am. Chem. Soc.* **1993**, *115* (14), 6420–6421. https://doi.org/10.1021/ja00067a071.
(58) Schweidler, S.; de Biasi, L.; Schiele, A.; Hartmann, P.; Brezesinski, T.; Janek, J. Volume Changes of Graphite Anodes Revisited: A Combined Operando X-Ray Diffraction and In Situ Pressure Analysis Study. *J. Phys. Chem. C* **2018**, *122* (16), 8829–8835. https://doi.org/10.1021/acs.jpcc.8b01873.
(59) Kim, J.; Middlemiss, D. S.; Chernova, N. A.; Zhu, B. Y. X.; Masquelier, C.; Grey, C. P. Linking Local Environments and Hyperfine Shifts: A Combined Experimental and Theoretical ^{31}P and ^{7}Li Solid-State NMR Study of Paramagnetic Fe(III) Phosphates. *J. Am. Chem. Soc.* **2010**, *132* (47), 16825–16840. https://doi.org/10.1021/ja102678r.
(60) Sampson, J. B.; Seitz, F. Theoretical Magnetic Susceptibilities of Metallic Lithium and Sodium. *Phys. Rev.* **1940**, *58* (7), 633–639. https://doi.org/10.1103/PhysRev.58.633.
(61) Stratford, J. M.; Kleppe, A. K.; Keeble, D. S.; Chater, P. A.; Meysami, S. S.; Wright, C. J.; Barker, J.; Titirici, M.-M.; Allan, P. K.; Grey, C. P. Correlating Local Structure and Sodium Storage in Hard Carbon Anodes: Insights from Pair Distribution Function Analysis and Solid-State NMR. *J. Am. Chem. Soc.* **2021**, *143* (35), 14274–14286. https://doi.org/10.1021/jacs.1c06058.
(62) Fujita, N.; Matsumoto, D.; Sakurai, Y.; Kawahara, K.; Ago, H.; Takenobu,

T.; Marumoto, K. Direct Observation of Electrically Induced Pauli Paramagnetism in Single-Layer Graphene Using ESR Spectroscopy. *Sci Rep* **2016**, *6* (1), 34966. https://doi.org/10.1038/srep34966.

(63) McRae, E.; Marêché, J. F. C-Axis Conductivity and Conductivity Anisotropy in Graphite Intercalation Compounds. *J. Mater. Res.* **1988**, *3* (1), 75–86. https://doi.org/10.1557/JMR.1988.0075.

(64) Strässler, S.; Pietronero, L. Intercalated Graphite: A Synthetic Metal II. Theory of Bond Length Change and Conductivity. In *Festkörperprobleme 21: Plenary Lectures of the Divisions "Semiconductor Physics" "Metal Physics" "Low Temperature Physics" "Thermodynamics and Statistical Physics" "Thin Films" "Magnetism" "Quantum Optics" of the German Physical Society Münster, March 9–14, 1981*; Treusch, J., Ed.; Advances in Solid State Physics; Springer: Berlin, Heidelberg, 1981; pp 313–324. https://doi.org/10.1007/BFb0108609.

(65) Hope, M. A.; Rinkel, B. L. D.; Gunnarsdóttir, A. B.; Märker, K.; Menkin, S.; Paul, S.; Sergeyev, I. V.; Grey, C. P. Selective NMR Observation of the SEI–Metal Interface by Dynamic Nuclear Polarisation from Lithium Metal. *Nat Commun* **2020**, *11* (1), 2224. https://doi.org/10.1038/s41467-020-16114-x.

(66) Leskes, M.; Kim, G.; Liu, T.; Michan, A. L.; Aussenac, F.; Dorffer, P.; Paul, S.; Grey, C. P. Surface-Sensitive NMR Detection of the Solid Electrolyte Interphase Layer on Reduced Graphene Oxide. *J. Phys. Chem. Lett.* **2017**, *8* (5), 1078–1085. https://doi.org/10.1021/acs.jpclett.6b02590.

(67) Jardón-Álvarez, D.; Leskes, M. Dynamic Nuclear Polarization in Inorganic Solids from Paramagnetic Metal Ion Dopants. In *Reference Module in Chemistry, Molecular Sciences and Chemical Engineering*; Elsevier, 2021. https://doi.org/10.1016/B978-0-12-823144-9.00027-3.

(68) Haber, S.; Rosy; Saha, A.; Brontvein, O.; Carmieli, R.; Zohar, A.; Noked, M.; Leskes, M. Structure and Functionality of an Alkylated LixSiyOz Interphase for High-Energy Cathodes from DNP-SsNMR Spectroscopy. *J. Am. Chem. Soc.* **2021**, *143* (12), 4694–4704. https://doi.org/10.1021/jacs.1c00215.

TOC figure

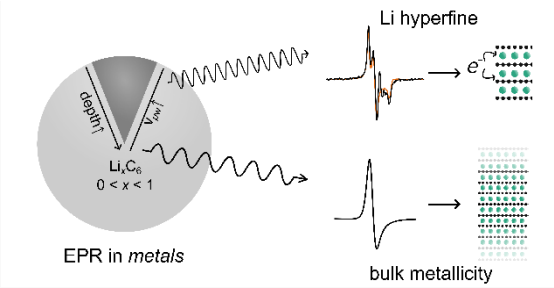
Li hyperfine
e^-
l_{skin}
l_{RF}
Li_xC_6
$0 < x < 1$
EPR in *metals*
bulk metallicity